RSC Advances

PAPER

View Article Online
View Journal | View Issue

Cite this: *RSC Adv.*, 2020, **10**, 26335

Hydroxyl porous aromatic frameworks for efficient adsorption of organic micropollutants in water†

Chen Mo,‡[a] Muhammad Faheem,‡[a] Saba Aziz,[a] Song Jian,[a] Wang Xue,[a] Tian Yuyang,*[a] Ding Shuang*[b] and Zhu Guangshan[a]

Environmental pollution is an important issue in sustainable human development. People give great importance to environmental protection, especially with regards to increasingly scarce water resources. Water pollution is becoming more and more serious due to the existence of organic micropollutants. As a platform with good stability, porous aromatic frameworks (PAFs) have been widely studied. Because of their high surface area and thermal stability, they are considered to be a good sewage treatment agent. However, the aromatic nature of PAFs makes their skeletons mostly hydrophobic. This characteristic of PAFs seriously affects their diffusion rate in water as an adsorbent, resulting in a low adsorption rate. In this work, we synthesized a series of hydroxyl functionalized porous aromatic frameworks (PAF-80, PAF-81, and PAF-82) *via* the Sonogashira–Hagihara cross-coupling reaction, which created polar motifs on the hydrophobic surfaces, and carried out adsorption tests on typical organic micropollutants in water such as bisphenol A (BPA), 2-naphthol (2-NO) and *p*-chloroxylenol (PCMX). Among the three PAFs, PAF-82 exhibited the highest BET surface area, polar active sites, and a high degree of conjugation, which led to the best adsorption performance compared to that of PAF-80 and PAF-81. The Langmuir adsorption capacity of PAF-82 for BPA, 2-NO, and PCMX is 689 mg g^{-1}, 431 mg g^{-1}, and 480 mg g^{-1}, respectively, which surpasses most previously reported adsorbents. In addition, after 5 cycles of regeneration, it still maintained a high removal rate for pollutants. The obtained results reveal that micropollutant adsorption in water is not controlled by a single factor, but is the result of a synergy of multiple factors, including specific surface area, polar functional groups, pore size distribution, and skeleton conjugation. Our study has revealed the great potential of hydroxyl PAFs for efficient adsorption of organic micropollutants in water.

Received 12th May 2020
Accepted 30th June 2020

DOI: 10.1039/d0ra04222f

rsc.li/rsc-advances

1 Introduction

Organic micropollutants have been widely detected in global water resources and have become a serious environmental problem around the world. Emerging organic micropollutants include linear aliphatic hydrocarbons, polycyclic aromatic hydrocarbons (PAH), polychlorinated biphenyls (PCBs), and synthetic resin raw materials such as bisphenol A, pharmaceuticals, and personal care products.[1,2] Due to the fact that they are low in concentration, toxic, and difficult to degrade in water, they pose a serious threat to human health.[3–6] Several methods have been designed to remove these microcontaminants, including photocatalytic degradation,[7–9] biodegradation,[10–12] oxidation, and physical adsorption.[13–16] In recent times, the adsorption method has been considered as a promising technology because of the ease of operation and low energy consumption.[17] Various solid adsorbents such as activated carbon[18,19] carbon nanotubes,[20] graphene oxide,[21] zeolites,[22] metal–organic frameworks (MOFs),[23] and covalent organic frameworks (COFs)[24–26] are widely used in the adsorption and degradation of organic micropollutants. However, due to their slow uptake, poor hydrolysis stability and poor reproducibility, their adsorption performance is restricted.[7,27] Therefore, developing porous materials with a high surface area, good hydrolytic stability, fast uptake, and excellent recyclability is of great significance for the removal of organic micropollutants from water and is becoming a field of interest. To achieve these advantages, a porous material should contain a covalent skeleton for better stability and the interaction between adsorbent and organic micropollutants should be strong. A common feature in all organic micropollutants is that they have different polar functional groups such as hydroxyl (–OH), carboxyl (–COOH), and amine ($–NH_2$) groups. It is possible to bind these

[a]*Key Laboratory of Polyoxometalate Science of the Ministry of Education, Faculty of Chemistry, Northeast Normal University, Changchun, 130024, P. R. China. E-mail: tianyy100@nenu.edu.cn*

[b]*Institute for Interdisciplinary Biomass Functional Materials Studies, Jilin Engineering Normal University, Changchun 130052, P. R. China. E-mail: dingshuang2018@163.com*

† Electronic supplementary information (ESI) available. See DOI: 10.1039/d0ra04222f

‡ Chen Mo and Muhammad Faheem contributed equally to this work.

pollutants through supramolecular interactions within the wall of the polar porous material.

In recent years, porous aromatic frameworks (PAFs) have been reported as an emerging class of porous materials due to their rigid framework, high surface area, and excellent stability. They are constructed through carbon–carbon bonds between aromatic building units.[28–30] Likewise, owing to the ease in which they can undergo framework modification as well as their excellent stability, aromatic-rich system, and permanent porosity, PAF materials could offer a unique platform for adsorbing organic micropollutants from water.[24,31–34] Particularly, the high surface area, aromatic skeleton, and specific polar functional groups of the framework may enhance adsorption capacity, affinity, and polarity of the porous materials for pollutants. It has been recognized that the hydroxyl (–OH) functional group has a progressive impact on pollutant adsorption.[35]

Keeping the above considerations in mind, we are presenting a series of hydroxyl (–OH) functionalized porous aromatic frameworks (PAF-80, PAF-81, and PAF-82) using phloroglucinol motifs and aromatic ethynyls as building units for organic micropollutant removal. These building units have the potential to offer unique binding sites, a high density of π-electrons, and chemical stability, which are essential for the adsorption of micro-contaminants. The integration of individual functional groups is an effective strategy to ameliorate the target property of PAFs. Introducing hydroxyl groups (–OH) onto the hydrophobic backbone of PAFs can greatly optimize the interactions between the PAF channel and organic micropollutants *via* hydrogen bonds. Moreover hydroxyl groups are capable of amending the channel polarity in the porous framework, which is also a key issue for aqueous pollution treatment.[36] On the other hand, high-density benzene rings in the porous framework improve the adsorption performance due to the π–π interactions with organic contaminants.[37] Taking this into account, we have decided to incorporate phloroglucinol and different aromatic ethynyl groups into the PAF walls. It is highly desirable to utilize the synergy of the high surface area, polar channels, and degree of conjugation of the material for the rapid adsorption of pollutants from water. The specific surface area, polar active sites, and excessive benzene rings of the material have a great influence on the adsorption capacity and adsorption rate, particularly the adsorption rate of organic micro-pollutants containing aromatic rings with polar pendant groups. This work emphasizes the importance of the synergy between the specific surface area, the interactions between the PAF channel and organic micropollutants, and the degree of conjugation of the materials for the adsorption of organic micropollutants in water.

2 Experimental

2.1. Chemicals and characterization

All chemicals and anhydrous solvents required for the synthesis were purchased from commercial sources and used without any further purification. 1,4-Diethynylbenzene, 1,3,5-triethynylbenzene, 1,3,5-tris(4-ethynylphenyl)benzene, tetrakis(triphenyl-phosphine)palladium and CuI were purchased from 3A Chemical. *N*,*N*-Dimethylformamide (DMF, 99.8%), bisphenol-A (BPA) ($C_{15}H_{16}O_2$, 98%), 2-hydroxynaphthalene ($C_{10}H_8O$, 98%) and PCMX (C_8H_9ClO, 98%) were purchased from Energy Chemical. Other reagents were purchased from Beijing Chemical Factory. PAF-80 was synthesized according to a previously reported procedure.[36] Fourier transform infrared spectroscopy (FTIR) was performed with KBr pellets in a wavelength range from 4000 to 400 cm^{-1} *via* the Nicolet-410 FT-IR spectrophotometer. Powder X-ray diffraction (PXRD) data were performed on a Siemens D5005 diffractometer in the range of 2–80° (2θ) with Cu Kα ($\lambda = 1.5418$ Å) radiation with a scanning rate of 5 °C min^{-1}. Thermogravimetric analysis (TGA) was measured on the Mettler Toledo thermal analyzer in the temperature range of 30–800 °C with a heating rate of 10 °C min^{-1} under an air atmosphere. The nitrogen adsorption–desorption isotherms were measured on an Autosorb (Quantachrome instrument) at 77 K from 0 to 1 bar relative pressure, and the pore size distribution (PSD) was obtained according to the NLDFT calculation model. Field emission scanning electron microscopic analysis (FESEM) was performed on a HITACHI SU8010 microscope. The UV-visible absorption spectroscopy was measured through the VARIAN Cary-60 UV-Visible spectrophotometer in the wavelength range of 200–800 nm.

2.2. Synthesis of PAF-80, PAF-81, and PAF-82

The synthetic procedure of novel PAF-81 and PAF-82 is similar to the procedure of PAF-80.[36] PAF-82 was synthesized using the tetrakis(triphenyl-phosphine) palladium-catalyzed Sonogashira–Hagihara cross-coupling chemical reaction. Typically, 1,3,5-trihydroxy-2,4,6-tribromobenzene (219 mg, 0.6 mmol), 1,3,5-tris(4-ethynylphenyl)benzene (227 mg, 0.6 mmol), tetrakis(triphenyl-phosphine) palladium (45 mg) and copper(I) iodide (15 mg) were placed in a 100 mL two-neck round bottom flask containing 30 mL of a mixed solvent of DMF and triethylamine (1 : 1 v/v), and degassed by three freeze–pump–thaw cycles. The reaction was maintained at 100 °C for 48 hours under N_2 atmosphere. After the reaction, the reaction mixture

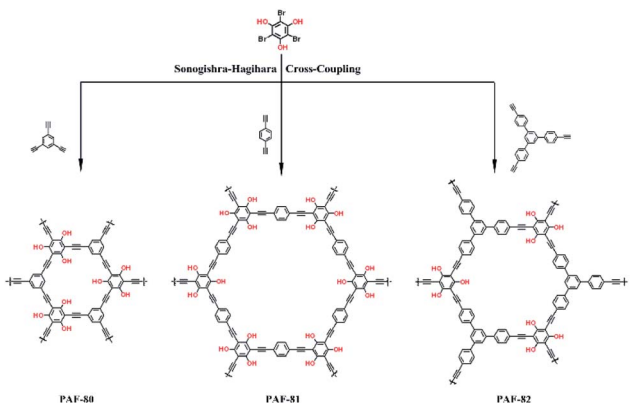

Scheme 1 The synthetic route and structures of PAF-80, PAF-81, and PAF-82.

was cooled to room temperature, and the resultant product was filtered, washed sequentially with 3 M HCl, water, DMF, and acetone to remove the catalyst and unreacted monomers. The product was then further purified by Soxhlet extraction with methanol for 48 h. After drying at 85 °C under vacuum for 12 h, PAF-82 was obtained as a brown powder. PAF-81 was also prepared through the same procedure, 1,4-diacetylenylbenzene (114 mg, 0.9 mmol) was used instead of 1,3,5-tris (4-ethynylphenyl) benzene, and the product was washed and dried to give a brownish-red colored polymer. The synthesis route is shown in Scheme 1.

2.3. Adsorption experiments

2.3.1 Adsorption kinetics. Adsorption kinetic studies of the organic micro-contaminants (BPA, 2NO, and PCMX) by PAF materials were carried out to evaluate their removal performance in water at room temperature (298 K). For this study, 3 mg of each adsorbent was added to 20 mL of contaminants (BPA, 2NO, and PCMX) in aqueous solution (0.1 mmol L^{-1}) and stirred with a magnetic bar. All adsorption experiments were performed under similar conditions. A syringe was used to draw a series of aliquots of the adsorbent and contaminant mixture at different adsorption times and filtered through a 0.22 μm hydrophilic filter membrane. The concentration of each contaminant before (0.1 mmol L^{-1}) and after the filtration process was analyzed by a UV-visible spectrophotometer based on a standard curve at a maximum absorbance wavelength (BPA at 276 nm, 2-NO at 274 nm and PCMX at 267 nm). The average of three parallel measurements was used for further adsorption kinetic fitting.

The removal efficiency of the tested contaminants (BPA, 2NO, and PCMX) by each adsorbent (PAF-80, PAF-82, and PAF-83) was calculated by the following equation:

$$\text{Removal efficiency} = \frac{C_0 - C_t}{C_0} \times 100\% \quad (1)$$

where C_0 (mmol L^{-1}) and C_t (mmol L^{-1}) represent the initial and remaining concentration of contaminants at specific times, respectively.

The adsorption capacity of the adsorbent towards organic contaminants was calculated by the following equation:

$$q_t = \frac{(C_0 - C_t) M_w V}{m} \quad (2)$$

where q_t (mg g^{-1}) is the amount of pollutant adsorbed by 1 g of adsorbent after the adsorption time t (min) and C_0 (mmol L^{-1}), and C_t (mmol L^{-1}) represent the initial and remaining concentration of pollutants after adsorption time t, respectively. M_w (g mol^{-1}) is the molar mass of pollutants, V (mL) is the volume of the contaminant solution and m (g) is the mass of the adsorbent.

The adsorption rate of the adsorbent is elucidated by the pseudo-second-order adsorption model of Ho and McKay, and the equation is as follows:

$$\frac{t}{q_t} = \frac{1}{q_e} + \frac{1}{k_{obs} q_e^2} \quad (3)$$

where q_t and q_e are the adsorption amounts of contaminants (mg g^{-1}) for a particular time t (min) that reached an equilibrium state, respectively, and k_{obs} is a second-order rate constant (g mg^{-1} min^{-1}).

2.3.2 Adsorption isotherms. For this study, 3 mg of each adsorbent was added to 20 mL of different contaminant concentrations ranging from 0.1 mmol to 1.0 mmol. After that, the mixtures were swiftly stirred or shaken at a constant speed for 24 h to ensure equilibrated adsorption over the PAFs. After 24 h, the treated samples were removed by filtration, and the concentration of the adsorption solution was measured using a UV-visible spectrophotometer.

The Langmuir adsorption model was adopted to fit the adsorption isotherm.[38] The equation is as follows:

$$\frac{1}{q_e} = \frac{1}{q_{max,e}} + \frac{1}{q_{max,e} kc} \quad (4)$$

where q_e (mg g^{-1}) is the amount of pollutant adsorbed at equilibrium, $q_{max,e}$ (mg g^{-1}) is the maximum adsorption capacity of the adsorbent at equilibrium, and c (mol L^{-1}) is the concentration of the residual pollutant. K (mol^{-1}) is the equilibrium constant.

2.3.3 Regeneration of the PAF materials. The PAF materials were simply soaked in ethanol for 3 h, which desorbed the tested contaminants and regenerated the polymer framework. Then the polymers were dried and reused to adsorb contaminants, which were cycled 5 times to evaluate their recyclability.

3 Results and discussion

As shown in Scheme 1, PAF-80, PAF-81, and PAF-82 possess similar porous architectures from the phloroglucinol motif-based building units linked through the Sonogashira–Hagihara cross-coupling reaction. This reaction process is primarily evidenced by Fourier-transform infrared (FT-IR) spectroscopy. Regarding PAF-80, PAF-81, PAF-82, and the corresponding monomers, the intense bands at 3265 cm^{-1} and 1068 cm^{-1} are ascribed to the stretching vibration of the terminal alkynyl group and the C–Br moieties in the monomers, respectively (Fig. S1†). The disappearance of the two intense bands is an indicator of the breakage of the C–H of the terminal alkyne and C–Br bonds, thus demonstrating the success and completion of a cross-coupling reaction between the monomers.[36] The broad IR band at 3420 cm^{-1} is the stretching vibration of the hydroxyl groups (–OH), which is similar to its monomer phloroglucinol. This confirms that the hydroxyl groups remain unchanged during the coupling reaction. The low-intensity bands at 2200 cm^{-1} for each PAF material are assigned to the stretching vibration mode of the alkyne (C≡C) moieties. Thermogravimetric analysis (TGA) was performed to examine the thermal stability of PAF-80, PAF-81, and PAF-82 (Fig. S2†). The observed TGA curves divulge that the PAF materials are thermally stable up to 400 °C. Also, no residue was observed above 800 °C, which shows the purity of the porous frameworks. The morphologies of the PAF materials (PAF-80, PAF-81, and PAF-82) were characterized by scanning electron microscopy (SEM) analysis. The SEM image of PAF-80 shows submicron particles,

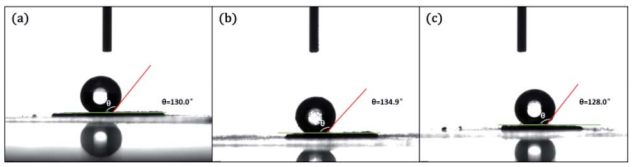

Fig. 1 Contact angle chart of (a) PAF-80, (b) PAF-81, and (c) PAF-82.

PAF-81 was petal-shaped, and PAF-82 consisted of beads of 0.5–1.0 μm (Fig. S3†). The broad peaks in the powder X-ray diffraction (PXRD) pattern of the PAF materials suggested that the series of polymers are amorphous (Fig. S4†). The UV-visible reflectance spectrum of the PAF materials (Fig. S5†) shows the difference in the conjugation. Compared to PAF-80 and PAF-81, PAF-82 produced a broader absorption spectrum in the long-wavelength region, which indicates that PAF-82 exhibits a stronger conjugated structure.[39]

The surface wettability of PAF-80, PAF-81, and PAF-82 was probed by contact angle measurements. As shown in Fig. 1, the observed contact angles of PAF-80, PAF-81, and PAF-82 were 130°, 134.9°, and 128°, respectively. The observed results suggested these hydroxyl PAFs possess similar surface wettability. Although the obtained PAF skeleton has polar groups in the channel, their surfaces are still hydrophobic due to excessive aromatic units in PAFs.

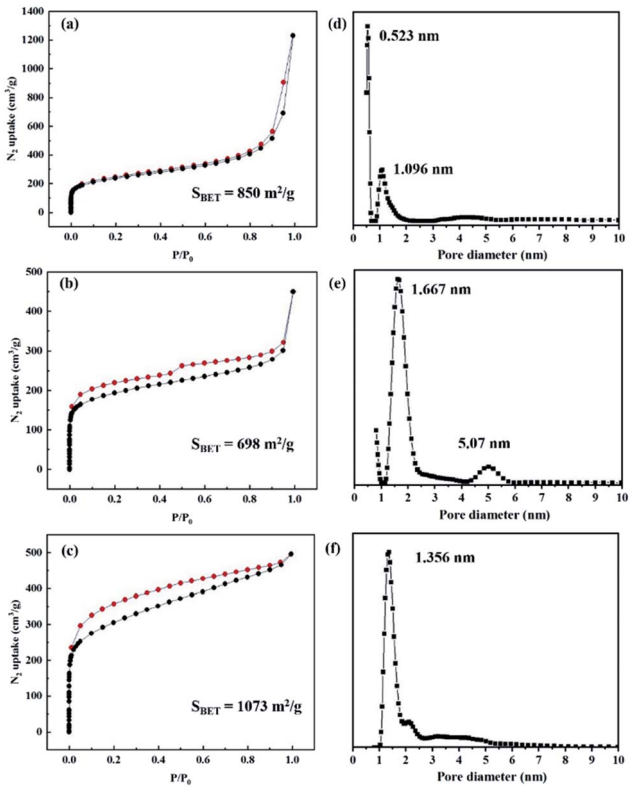

Fig. 2 (a–c) N_2 adsorption–desorption isotherms of PAF-80, PAF-81 and PAF-82. (d–f) Pore size distribution (PSD) of PAF-80, PAF-81 and PAF-82 using the NLDFT model.

N_2 adsorption–desorption analysis was performed at 77 K to investigate the textural properties of the PAF materials. Each PAF material was activated at 100 °C for 12 h to remove guest molecules from the channels. As shown in Fig. 2, the N_2 sorption isotherm of PAF-80 shows a typical type I adsorption curve with high nitrogen uptake at low relative pressure, indicating microporous characteristics (Fig. 2a). The N_2 sorption isotherm of PAF-81 displays a typical type IV adsorption curve. There is a slight lag between the adsorption and desorption branches, which indicates the existence of mesopores in PAF-81 (Fig. 2b). As indicated in Fig. 2c, PAF-82 does not show a classic type I isotherm and a steady linear increase is observed in the high-pressure zone. Also, a low-pressure hysteresis is observed between the adsorption and desorption curves. This low-pressure hysteresis may occur due to expansion caused by the softness of the material.[40] The surface areas of the PAF materials were calculated using the Brunauer–Emmett–Teller (BET) model. The observed surface areas of PAF-80, PAF-81, and PAF-82 are 850 $m^2\ g^{-1}$, 698 $m^2\ g^{-1}$, and 1073 $m^2\ g^{-1}$, respectively

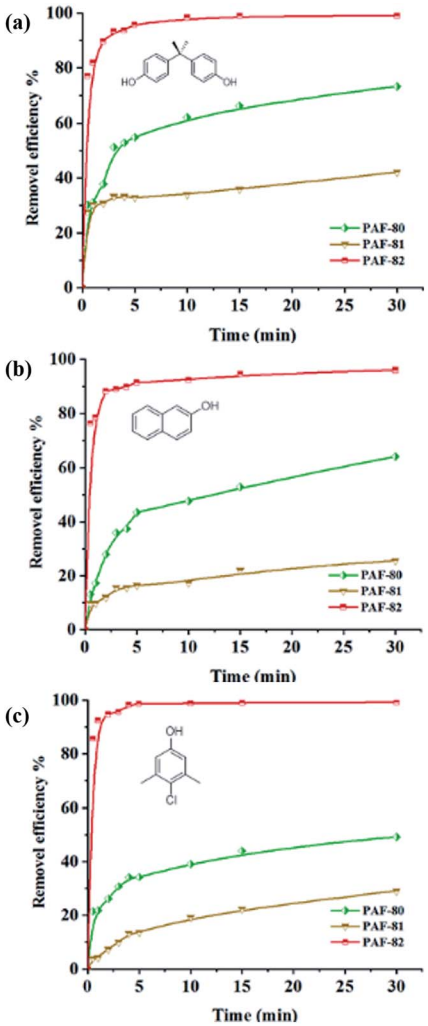

Fig. 3 Kinetic adsorption curve of 0.1 mM (a) bisphenol A, (b) 2-naphthol, and (c) *p*-chloroxylenol by 0.15 mg mL^{-1} PAFs over time. The structural formulas of the tested pollutants are shown in the figure.

(Fig. 2a–c). The surface areas follow the order PAF-82 > PAF-80 > PAF-81. Moreover, the pore size distribution (PSD) of the PAF materials was calculated by using non-local density functional theory (NLDFT). The observed pore sizes of PAF-80, PAF-81, and PAF-82 are centered at 0.523 nm/1.096 nm, 1.667 nm/5.07 nm, and 1.356 nm, respectively (Fig. 2d–f).

After the successful formation of the desired PAF materials (PAF-80, PAF-81, and PAF-82), their capabilities to remove organic micropollutants from water through adsorption were explored. Three different typical phenolic contaminants (bisphenol A, 2-naphthol, and *p*-chloroxylenol), which are carcinogenic, difficult to degrade in water, and known to disrupt the human endocrine and nervous system, as well as causing other serious health problems even at low concentrations,[41] were selected as model micropollutants to evaluate the adsorption performance of the PAF materials. All the adsorption experiments were performed under the same conditions. Aqueous solutions of BPA, 2-NO, and PCMX showed an absorption maximum at 276 nm, 274 nm, and 267 nm, respectively. The removal performance of PAF-80, PAF-81, and PAF-82 was determined using the UV-visible spectra (Fig. S6†). As indicated, the UV-visible absorption intensities of the solutions decrease with time, which infers a decrease in pollutant (BPA, 2-NO, and PCMX) concentrations due to adsorption by the PAF materials, confirming the good removal capability. Importantly, the observed adsorption response is different for different PAFs. As a result, the observed removal efficiencies of PAF materials towards the three contaminants were surprisingly different.

To determine the removal efficiency of the materials, the adsorption rate and saturated adsorption time are important. The adsorption rate of BPA, 2-NO, and PCMX onto PAF-80, PAF-81, and PAF-82 as a function of time is shown in Fig. 3. As indicated in Fig. 3a, the removal efficiency of PAF-82 towards bisphenol A (BPA) acquired 77% in the initial 30 s and equilibrium was reached after 15 minutes. After equilibrium, the removal rate reached 99%. On the contrary, PAF-80 and PAF-81 had removal efficiencies of only 30% and 27% after the initial 30 s, requiring 45 min and 60 min to achieve adsorption equilibrium, respectively. Moreover, the removal efficiency of PAF-82 towards 2-naphthol (2-NO) reached 76% within 30 s and equilibrium was achieved after 30 minutes. After equilibrium, the removal efficiency reached 96%, which is higher than the removal rate of PAF-80 as well as PAF-81 (Fig. 3b). Likewise, the removal efficiency of PAF-82 for *p*-chloroxylenol (PCMX) reached 86% within 30 s, and the adsorption equilibrium was attained in 10 minutes with a removal efficiency of 99%. In contrast, PAF-80 and PAF-81 removed only 21% and 4% in the initial 30 s, requiring 30 min and 45 min to achieve adsorption equilibrium, respectively (Fig. 3c). The removal efficiencies or removal rates toward the three micro-pollutants are all above 96%, suggesting that PAF-82 exhibits the fastest adsorption rate as compared to PAF-80 and PAF-81 and can remove traces of contaminants from water. Fast adsorption rates of the PAF materials could be obtained in the first 10 min because of the many available adsorption sites in the initial stage. Then, the adsorption rate becomes slow until the adsorption equilibrium. From the removal rate curve, the order of removal efficiency towards pollutant molecules by the three materials is PAF-82 > PAF-80 > PAF-81.

The kinetic data was further explored by the pseudo-second-order kinetic model of Ho and McKay. Their linear fitting curves are displayed in Fig. S7.† The fitting curves, correlation coefficients (R^2), and the rate constant (K_{obs}) values suggested that the pseudo-second-order model could better describe the adsorption kinetics of BPA, 2-NO, and PCMX onto PAF-80, PAF-81, and PAF-82, respectively. The calculated kinetic parameters and adsorption rates are summarized in Table S1.†

Adsorption isotherms, which are useful for understanding the maximum adsorption capacity and the interaction between adsorbate and adsorbent, were applied to probe the adsorption performance of the PAF materials. The adsorption isotherms for BPA, 2-NO, and PCMX onto PAF-80, PAF-81, and PAF-82 are shown in Fig. S8.† The isotherm data were analyzed by the Langmuir isotherm model. The linear fitting curves are shown in Fig. S9.† The obtained isotherm parameters are summarized in Table 1. According to the correlation coefficient (R^2) value and fitted curves, the adsorption isotherms of the tested micropollutants by PAF-80, PAF-81, and PAF-82 are all fitted better with the Langmuir model, suggesting possible monolayer adsorption and specific homogeneous sites within the adsorbent.[34] The adsorption behaviors of our PAF materials towards three pollutant molecules are not the same. As shown in Table 1, PAF-82 exhibits a maximum adsorption capacity of 689 mg g^{-1} for bisphenol A (BPA). On the contrary, PAF-80 and PAF-81 exhibit an adsorption capacity of 378 and 138 mg g^{-1}, respectively. For the adsorption of 2-naphthol (2-NO), the maximum adsorption capacity of PAF-82 was 431 mg g^{-1}, which is higher than PAF-80 (200 mg g^{-1}) and PAF-81 (155 mg g^{-1}). Likewise, we perceived a similar trend even for the adsorption of *p*-chloroxylenol (PCMX), PAF-82 had a maximum adsorption capacity of 480 mg g^{-1}, while those of PAF-80 and PAF-81 were 235 mg g^{-1} and 163 mg g^{-1}, respectively. Remarkably, the order of the adsorption capacities towards pollutant molecules by the three materials is PAF-82 > PAF-80 > PAF-81, which is consistent with their order of specific surface areas.

Table 1 Langmuir isotherm model parameters for the adsorption of micropollutant by PAFs

Sorbent	Pollutant	$q_{max,e}$[a] (mg g^{-1})	K^b (L mol^{-1})	R^{2c}
PAF-80	BPA	378	8686	0.9869
PAF-81		138	5077	0.9874
PAF-82		689	50 379	0.9739
PAF-80	2-NO	200	6602	0.9918
PAF-81		155	1858	0.9989
PAF-82		431	33 342	0.9881
PAF-80	PCMX	235	10 485	0.9988
PAF-81		163	5033	0.9965
PAF-82		480	30 833	0.9978

[a] The maximum adsorption capacity calculated by the Langmuir model. [b] The Langmuir constant related to the energy of adsorption. [c] The correlation coefficients of the Langmuir isotherm model.

The prime feature of the different adsorption results is that the specific surface area of the PAF materials was different. Among the three PAF materials, PAF-82 exhibits the fastest adsorption capacity and removal efficiency towards the three pollutant molecules. This can be attributed to the fact that PAF-82 has a higher surface area than PAF-80 and PAF-81. The high surface area of the material increases the interaction probability while the polar hydroxyl groups create a strong affinity with polar organic microcontaminants in water to achieve an efficient adsorption performance. Also, we believe that the high adsorption capacity of PAF-82 as compared to PAF-80 and PAF-81 is due to the high degree of conjugation in the PAF-82 skeleton. The excessive benzene rings in the PAF-82 skeleton produce π–π interactions with the benzene ring of the organic pollutant molecules, which leads to the best adsorption performance. Besides, we found that the adsorption performance of PAF-80 was superior to PAF-81, this observation revealed that the higher surface area and smaller pore size of PAF-80 may be related to the high adsorption capacity and removal rate as compared to PAF-81. For convenience, the average molecular sizes of BPA, 2-NO, and PCMX are shown in Fig. S10.† From the previous discussion, we conclude that the excellent adsorption performance of PAF-82 towards organic micropollutants in water is not controlled by a single factor, but is the result of the combined action of multiple factors such as specific surface area, polar active sites, pore size, and the degree of conjugation of the skeleton.

The recyclability of the adsorbent is also an important indicator for evaluating its performance. In this work, ethanol can be used to simply regenerate the adsorbed material.

Adsorption/desorption experiments were carried out 5 times in succession. The recycling test demonstrated that after 5 cycles there was absolutely no loss in the adsorption capacity of PAF-82 (Fig. 4), which suggests the excellent recyclability of PAF-82 in the removal of organic micropollutants (BPA, 2-NO, and PCMX) from water by adsorption. Meanwhile, due to the good stability of the PAFs, the adsorbed micropollutants can be removed by direct heating (as shown in Fig. S11†). The TGA results indicate that the adsorbed chemicals were completely removed before the temperature increased to 300 °C as the adsorbents are thermally stable at this stage. Therefore, different recycling methods can be selected to regenerate the hydroxyl PAFs depending on practical requirements.

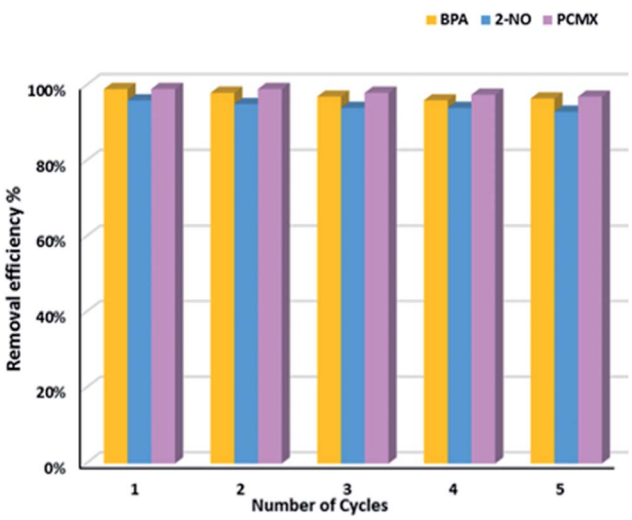

Fig. 4 Histogram of pollutant removal efficiency of PAF-82 after five adsorption/desorption cycles.

4 Conclusions

In summary, a series of hydroxyl functionalized PAF materials (PAF-80, PAF-81, and PAF-82) were designed and synthesized from phloroglucinol motifs with two and three-node aromatic ethynyls by using the Sonogashira–Hagihara cross-coupling reaction. The obtained porous frameworks contain polar functional groups, π-electron-rich benzene units, and chemical stability, which are essential for the adsorption of polar organic micropollutants. Three different typical phenolic contaminants (bisphenol A, 2-naphthol, and *p*-chloroxylenol), were selected as model micro-pollutants to evaluate the adsorption performance of the PAFs. In this investigation, among the three PAFs, PAF-82 exhibits the highest BET surface area (1073 $m^2\ g^{-1}$), apposite pore sizes, and a strong degree of conjugation (a wider UV absorption peak at a longer wavelength), which led to the best adsorption performance compared to that of PAF-80 and PAF-81. The calculated adsorption capacity of PAF-82 for BPA, 2-NO, and PCMX is 689 mg g^{-1}, 431 mg g^{-1}, and 480 mg g^{-1}, respectively, which surpasses most of the previously reported adsorbents. This work proves that the adsorption performance of PAF materials towards organic micropollutants in water is not controlled by a single factor, but is the result of a synergy of multiple factors such as specific surface area, polar active sites, pore size, and the degree of conjugation of the porous skeleton. Benefiting from the intrinsic stability of its very robust framework, PAF-82 showed excellent recyclability after 5 adsorption/desorption cycles. Therefore, PAF-82 could be a potential adsorbent for organic micro-contaminants in water.

Conflicts of interest

The authors declare no competing financial interest.

Acknowledgements

The authors gratefully acknowledge the financial support from the National Natural Science Foundation of China (21531003 and 21601031), the Fundamental Research Funds for the Central Universities (2412019FZ011), Jilin Engineering Normal University PhD Startup Foundation (No. BSKJ201829) and Jilin Engineering Normal University General Intramural Foundation (No. XYB201822).

Notes and references

1 A. Alsbaiee, B. J. Smith, L. Xiao, Y. Ling, D. E. Helbling and W. R. Dichtel, *Nature*, 2016, **529**, 190–194.

2 R. Jiang, J. Liu, B. Huang, X. Wang, T. Luan and K. Yuan, *Sci. Total Environ.*, 2020, **714**, 136689.
3 C. Barrios-Estrada, M. de Jesus Rostro-Alanis, B. D. Munoz-Gutierrez, H. M. N. Iqbal, S. Kannan and R. Parra-Saldivar, *Sci. Total Environ.*, 2018, **612**, 1516–1531.
4 Z. He, Q. Zhang, Z. Wei, Y. Zhao and X. Pan, *Sci. Total Environ.*, 2019, **690**, 417–425.
5 B. Petrie, R. Barden and B. Kasprzyk-Hordern, *Water Res.*, 2015, **72**, 3–27.
6 S. I. Bonfoh, D. Li, X. Xiong, Z. Du, C. Xiong and H. Jiang, *Talanta*, 2020, **210**, 120661.
7 S. W. Lv, J. M. Liu, N. Zhao, C. Y. Li, Z. H. Wang and S. Wang, *J. Hazard. Mater.*, 2020, **387**, 122011.
8 J. Wang, X. Shao, J. Liu, X. Ji, J. Ma and G. Tian, *Ecotoxicol. Environ. Saf.*, 2020, **190**, 110139.
9 X. Zheng, Q. Zhang, T. Chen, Y. Wu, J. Hao, C. Tan, P. Chen, F. Wang, H. Liu, W. Lv and G. Liu, *J. Hazard. Mater.*, 2020, **386**, 121961.
10 N. X. Feng, J. Yu, C. H. Mo, H. M. Zhao, Y. W. Li, B. X. Wu, Q. Y. Cai, H. Li, D. M. Zhou and M. H. Wong, *Sci. Total Environ.*, 2018, **616–617**, 117–127.
11 X. Su, S. Li, J. Cai, Y. Xiao, L. Tao, M. Z. Hashmi, H. Lin, J. Chen, R. Mei and F. Sun, *Sci. Total Environ.*, 2019, **688**, 917–925.
12 B. Suyamud, D. Inthorn, B. Panyapinyopol and P. Thiravetyan, *Water, Air, Soil Pollut.*, 2018, **229**, 348.
13 Z. Guo, J. Zhang, Y. Kang and H. Liu, *Ecotoxicol. Environ. Saf.*, 2017, **145**, 442–448.
14 K. Tang, Y. Li, X. Zhang, M. Li, Q. Du, H. Li, Y. Wang, D. Wang, C. Wang, K. Sui, H. Li and Y. Xia, *J. Appl. Polym. Sci.*, 2019, **137**, 48315.
15 D. Banerjee, P. Bhowmick, D. Pahari, S. Santra, S. Sarkar, B. Das and K. K. Chattopadhyay, *Phys. E*, 2017, **87**, 68–76.
16 M. Del Rio, G. Turnes Palomino and C. Palomino Cabello, *ACS Appl. Mater. Interfaces*, 2020, **12**, 6419–6425.
17 T. Rasheed, M. Bilal, F. Nabeel, M. Adeel and H. M. N. Iqbal, *Environ. Int.*, 2019, **122**, 52–66.
18 Z. Li, M. A. Gondal and Z. H. Yamani, *Saudi Chemical Society*, 2014, **18**, 208–213.
19 H. Soni and P. Padmaja, *J. Porous Mater.*, 2014, **21**, 275–284.
20 S. Li, Y. Gong, Y. Gang, C. He, L. Hu, L. Zhu, L. Sun and D. Shu, *Chem. Eng. J.*, 2015, **260**, 231–239.
21 S. Bele, V. Samanidou and E. Deliyanni, *Chem. Eng. Res. Des.*, 2016, **109**, 573–585.
22 N. Gene, O. Kilicoglu and A. O. Narci, *Environ. Technol.*, 2017, **38**, 424–432.
23 F. Qin, S. Jia, Y. Liu, H. Li and S. Wu, *Desalin. Water Treat.*, 2015, **54**, 93–102.
24 J. Y. Yue, L. Wang, Y. Ma, P. Yang, Y. Q. Zhang, Y. Jiang and B. Tang, *Dalton Trans.*, 2019, **48**, 17763–17769.
25 L. Huang, N. Mao, Q. Yan, D. Zhang and Q. Shuai, *ACS Appl. Nano Mater.*, 2019, **3**, 319–326.
26 D. Wei, J. Li, Z. Chen, L. Liang, J. Ma, M. Wei, Y. Ai and X. Wang, *J. Mol. Liq.*, 2020, **301**, 112431.
27 D. Zhao, Y. Tian, X. Jing, Y. Lu and G. Zhu, *J. Mater. Chem. A*, 2019, **7**, 157–164.
28 T. Ben, H. Ren, S. Ma, D. Cao, J. Lan, X. Jing, W. Wang, J. Xu, F. Deng, J. M. Simmons, S. Qiu and G. Zhu, *Angew. Chem., Int. Ed. Engl.*, 2009, **48**, 9457–9460.
29 L. Jiang, Y. Tian, T. Sun, Y. Zhu, H. Ren, X. Zou, Y. Ma, K. R. Meihaus, J. R. Long and G. Zhu, *J. Am. Chem. Soc.*, 2018, **140**, 15724–15730.
30 M. Li, H. Ren, F. Sun, Y. Tian, Y. Zhu, J. Li, X. Mu, J. Xu, F. Deng and G. Zhu, *Adv. Mater.*, 2018, **30**, 1804169.
31 Y. Yuan and G. Zhu, *ACS Cent. Sci.*, 2019, **5**, 409–418.
32 J. Kamcev, M. K. Taylor, D. M. Shin, N. N. Jarenwattananon, K. A. Colwell and J. R. Long, *Adv. Mater.*, 2019, **31**, e1808027.
33 Y. Yuan, Q. Meng, M. Faheem, Y. Yang, Z. Li, Z. Wang, D. Deng, F. Sun, H. He, Y. Huang, H. Sha and G. Zhu, *ACS Cent. Sci.*, 2019, **5**, 1432–1439.
34 R. Zhao, T. Ma, S. Li, Y. Tian and G. Zhu, *ACS Appl. Mater. Interfaces*, 2019, **11**, 16662–16673.
35 J. Xu, L. Wang and Y. Zhu, *Langmuir*, 2012, **28**, 8418–8425.
36 X. Shen, M. Faheem, Y. Matsuo, S. Aziz, X. Zhang, Y. Li, J. Song, Y. Tian and G. Zhu, *J. Mater. Chem. A*, 2019, **7**, 2507–2512.
37 W. Xie, D. Cui, S.-R. Zhang, Y.-H. Xu and D.-L. Jiang, *Mater. Horiz.*, 2019, **6**, 1571–1595.
38 I. X. Garcia-Zubiri, G. Gonzalez-Gaitano and J. R. Isasi, *J. Colloid Interface Sci.*, 2009, **337**, 11–18.
39 Y. Byun and A. Coskun, *Chem. Mater.*, 2015, **27**, 2576–2583.
40 H. Ren, T. Ben, F. Sun, M. Guo, X. Jing, H. Ma, K. Cai, S. Qiu and G. Zhu, *J. Mater. Chem.*, 2011, **21**, 10348–10353.
41 P. W. Seo, N. A. Khan, Z. Hasan and S. H. Zhung, *ACS Appl. Mater. Interfaces*, 2016, **8**, 29799–29807.